

Spurious modes in geometrically nonlinear small displacement finite elements with incompatible modes



Theodore Sussman^a, Klaus-Jürgen Bathe^{b,*}

^aADINA R & D, Inc., Watertown, MA 02472, United States

^bMassachusetts Institute of Technology, Cambridge, MA 02139, United States

ARTICLE INFO

Article history:

Received 15 March 2014

Accepted 16 April 2014

Keywords:

Incompatible finite elements

Spurious modes

Small displacements

Small strains

Geometrically nonlinear analysis

Critical strain value

ABSTRACT

We demonstrate the existence of spurious modes in finite elements with incompatible modes when a geometrically nonlinear displacement analysis with small displacements and strains is performed. The spurious modes are a direct consequence of the incompatibility of the elements with displacement boundary conditions. We derive a critical compressive strain condition analytically, and show that the critical strain can be quite small, with small displacements, if the geometric aspect ratio of the elements is large but still practical. In numerical examples we give further insight and results in correspondence with the analytical theory, and demonstrate that spurious modes can be triggered in practical small strain analyses when using elements with incompatible modes.

© 2014 Elsevier Ltd. All rights reserved.

1. Introduction

The two-dimensional 4-node and three-dimensional 8-node incompatible modes finite elements (here now referred to as ICM elements) have been proposed in Ref. [1], improved for element geometric distortions in Ref. [2] and extensively used for many years. As the formulation of the ICM elements is quite well known, we do not give the formulation details here; for a general description of the elements, see for example Ref. [3]. The key advantage of these elements, as compared with the elements not containing incompatible modes, is that the ICM elements do not exhibit shear locking when subjected to pure bending. The undistorted ICM elements pass the linear analysis patch tests, and, with proper corrections, the distorted elements also pass these tests [2,3].

The elements are in fact a special case of the ‘enhanced strain elements’ (referred to as EAS elements) proposed in Ref. [4] and extensively studied, see for example Refs. [5–11] and the references therein. The concept of enhancing the strain assumptions in finite elements is quite appealing to avoid locking phenomena but it was also shown that the EAS elements, and hence ICM elements, are in fact unstable in *large strain* conditions [8–10]. To remedy the behavior of the elements, a stabilization technique was proposed [11] with the use of deformation dependent stabilization parameters. While perhaps useful,

however, in our developments of finite element procedures we prefer to not use such factors [3,12].

Although the ICM elements are perhaps best suited to model pure bending, in practice the elements are used in very complex nonlinear analyses in which the elements are subjected to a wide variety of stresses and boundary conditions. Thus it is valuable to understand the behavior of these elements in as many situations as possible. In fact, the present paper is motivated by an attempt to explain the unexpected and unphysical results obtained in the analysis of a large industrial problem involving only small strains.

The purpose of the present paper is to demonstrate the existence of spurious modes (displacement patterns with zero or negative energy) in meshes of geometrically nonlinear ICM elements subjected to *only small displacement and small strain conditions*. The spurious modes are associated with the incompatibility of the incompatible modes with the boundary conditions, and the spurious modes are triggered when the strains reach a certain critical value. The critical value is highly dependent on the element geometric aspect ratios, with elements having a large aspect ratio giving a small critical value.

In Section 2, we derive the tangent bending modulus of a two-dimensional undistorted rectangular 4-node ICM element, assuming geometric nonlinear conditions, and a linear elastic material with zero Poisson’s ratio. The theoretical results show that even in small displacements only, the element can become unstable.

In Section 3, we present some numerical examples that illustrate and give insight into the derived theoretical results, and that

* Corresponding author. Tel.: +1 6179265199.

E-mail address: kjb@mit.edu (K.J. Bathe).

show the spurious modes for various element assemblages in two- and three-dimensional analyses. We also include the results of a practical analysis case.

Finally we give some closing remarks in Section 4.

2. Derivation of the element critical strain criterion

In the derivation of the critical strain condition, we make various simplifying assumptions in order to have a clear derivation and obtain insight into the reasons for the instability to occur. These assumptions will be introduced during the derivation.

The principle of virtual work for the total Lagrangian formulation is [3]

$$\delta W = \int S_{ij} \delta \varepsilon_{ij} dV \quad (1)$$

where δW is the virtual work, S_{ij} is the 2nd Piola–Kirchhoff stress tensor, referred to the original configuration, ε_{ij} is the Green–Lagrange strain tensor, referred to the original configuration and the integral is performed over the original volume. For brevity, we have dropped the left super- and subscripts commonly used to indicate the time and reference configuration [3].

The increment in the principle of virtual work can be written

$$\Delta \delta W = \int \left(\frac{\partial S_{ij}}{\partial \varepsilon_{kl}} \Delta \varepsilon_{kl} \delta \varepsilon_{ij} + S_{ij} \Delta \delta \varepsilon_{ij} \right) dV \quad (2)$$

where the Δ denotes an increment.

In the following we assume small strain conditions with linear isotropic elasticity, Poisson’s ratio equal to zero and planar deformations in the x_1 – x_2 plane. Eq. (2) becomes

$$\Delta \delta W = \int (E(\Delta \varepsilon_{11} \delta \varepsilon_{11} + \Delta \varepsilon_{22} \delta \varepsilon_{22}) + 4G \Delta \varepsilon_{12} \delta \varepsilon_{12} + S_{11} \Delta \delta \varepsilon_{11} + S_{22} \Delta \delta \varepsilon_{22} + 2S_{12} \Delta \delta \varepsilon_{12}) dV \quad (3)$$

in which $S_{11} = E \varepsilon_{11}$, $S_{22} = E \varepsilon_{22}$, $S_{12} = 2G \varepsilon_{12}$ and the symmetries of S_{ij} and ε_{ij} are employed.

Using the definition $\varepsilon_{ij} = \frac{1}{2}(u_{i,j} + u_{j,i} + u_{k,i} u_{k,j})$ where $u_{i,j} = \frac{\partial u_i}{\partial x_j}$, u_i are the displacement components, x_i are the (original) coordinate components, and k is an index used in conjunction with the Einstein summation convention, we obtain for small strains

$$\varepsilon_{11} \approx u_{1,1}, \varepsilon_{22} \approx u_{2,2}, \quad \varepsilon_{12} \approx \frac{1}{2}(u_{1,2} + u_{2,1}) \quad (4a, b, c)$$

$$\Delta \varepsilon_{11} \approx \Delta u_{1,1}, \quad \Delta \varepsilon_{22} \approx \Delta u_{2,2}, \quad \Delta \varepsilon_{12} \approx \frac{1}{2}(\Delta u_{1,2} + \Delta u_{2,1}) \quad (5a, b, c)$$

$$\Delta \delta \varepsilon_{11} = \Delta u_{1,1} \delta u_{1,1} + \Delta u_{2,1} \delta u_{2,1}, \quad \Delta \delta \varepsilon_{22} = \Delta u_{1,2} \delta u_{1,2} + \Delta u_{2,2} \delta u_{2,2},$$

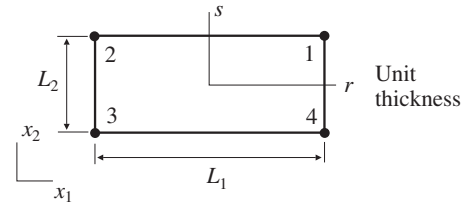
$$\Delta \delta \varepsilon_{12} = \frac{1}{2}(\Delta u_{1,1} \delta u_{1,2} + \Delta u_{2,1} \delta u_{2,2} + \Delta u_{1,2} \delta u_{1,1} + \Delta u_{2,2} \delta u_{2,1}) \quad (6a, b, c)$$

so that Eq. (3) becomes

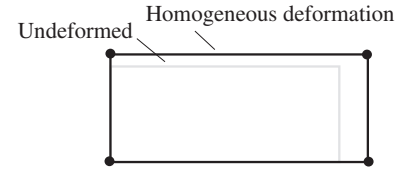
$$\Delta \delta W = \int E(\Delta u_{1,1} \delta u_{1,1} + \Delta u_{2,2} \delta u_{2,2}) dV + \int G(\Delta u_{1,2} \delta u_{1,2} + \Delta u_{2,1} \delta u_{2,1} + \Delta u_{2,1} \delta u_{1,2} + \Delta u_{1,2} \delta u_{2,1}) dV$$

$$+ \int S_{11}(\Delta u_{1,1} \delta u_{1,1} + \Delta u_{2,1} \delta u_{2,1}) dV + \int S_{22}(\Delta u_{1,2} \delta u_{1,2} + \Delta u_{2,2} \delta u_{2,2}) dV + \int S_{12}(\Delta u_{1,1} \delta u_{1,2} + \Delta u_{2,1} \delta u_{2,2} + \Delta u_{1,2} \delta u_{1,1} + \Delta u_{2,2} \delta u_{2,1}) dV \quad (7)$$

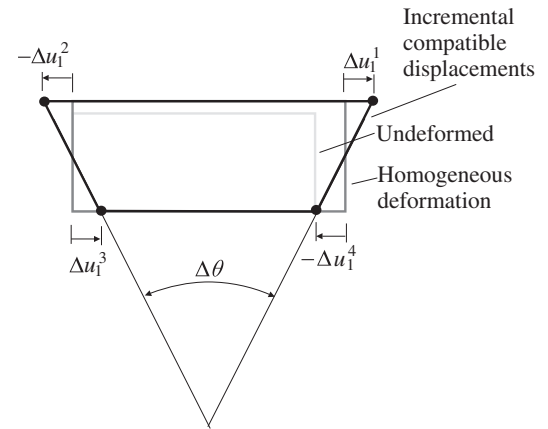
We now consider the single rectangular two-dimensional 4-node ICM element shown in Fig. 1. This element is first subjected to a homogeneous deformation that produces the stresses S_{11} ,



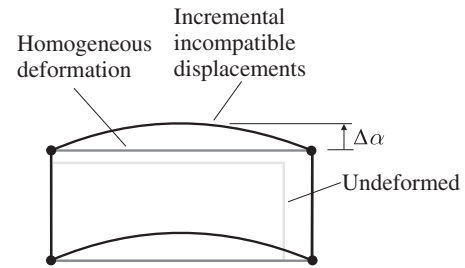
(a) Initial configuration



(b) Homogeneous deformation applied



(c) Incremental bending applied, compatible displacements shown



(d) Incompatible displacements due to incremental bending

Fig. 1. 2D 4-node ICM element under homogeneous deformation and incremental bending.

S_{22} , S_{12} . Since this deformation is homogeneous, the incompatible modes in the element are not triggered.

Now consider the following incremental nodal displacements: $\Delta u_1^1 = \Delta u_1^3 = \frac{L_2}{4} \Delta \theta$, $\Delta u_1^2 = \Delta u_1^4 = -\frac{L_2}{4} \Delta \theta$ in which the superscript denotes the node number and in which $\Delta \theta$ controls the magnitude of the displacement. Here $\Delta \theta$ represents an incremental rotation as shown in the figure (assuming small strains, the original value of L_2 is used instead of the deformed value). The incremental nodal displacements cause an internal incremental displacement within the element of

$$\Delta u_1 = \frac{L_2}{4} r s \Delta \theta \quad (8)$$

where r, s are the element isoparametric coordinates.

Simultaneously, an incremental incompatible displacement of

$$\Delta u_2 = (1 - r^2) \Delta \alpha \quad (9)$$

is introduced, where $\Delta \alpha$ is the magnitude of the incremental incompatible mode ($\Delta \alpha$ represents a length rather than an angle; α is customarily used to represent the magnitude of an incompatible mode). Thus there are two independent incremental degrees of freedom, $\Delta \theta$ and $\Delta \alpha$, and two corresponding variations, $\delta \theta$ and $\delta \alpha$.

Since the element is rectangular, we do not need to include the corrections to the incompatible modes shape functions required for the element to pass the patch test.

Clearly

$$\begin{aligned} \Delta u_{1,1} &= \frac{L_2}{2L_1} s \Delta \theta, & \Delta u_{1,2} &= \frac{1}{2} r \Delta \theta, \\ \Delta u_{2,1} &= -\frac{4}{L_1} r \Delta \alpha, & \Delta u_{2,2} &= 0 \end{aligned} \quad (10a, b, c, d)$$

Using Eqs. (5), (6) and (10), and performing the indicated integrals, Eq. (7) becomes in matrix form

$$\Delta \delta W = \begin{bmatrix} \delta \theta & \delta \alpha \end{bmatrix} \begin{bmatrix} k_{11} & k_{12} \\ k_{12} & k_{22} \end{bmatrix} \begin{bmatrix} \Delta \theta \\ \Delta \alpha \end{bmatrix} \quad (11)$$

where

$$\begin{aligned} k_{11} &= (E + S_{11}) \frac{L_2^3}{12L_1} + (G + S_{22}) \frac{L_1 L_2}{12} \\ k_{12} &= -\frac{2L_2}{3} G \\ k_{22} &= (G + S_{11}) \frac{16L_2}{3L_1} \end{aligned} \quad (12a, b, c)$$

The incremental forces conjugate to the incremental displacements are thus

$$\begin{bmatrix} \Delta F_\theta \\ \Delta F_\alpha \end{bmatrix} = \begin{bmatrix} k_{11} & k_{12} \\ k_{12} & k_{22} \end{bmatrix} \begin{bmatrix} \Delta \theta \\ \Delta \alpha \end{bmatrix} \quad (13)$$

Using the condition $\Delta F_\alpha = 0$ we obtain

$$\Delta F_\theta = k \Delta \theta \quad (14)$$

where

$$k = k_{11} - \frac{k_{12}^2}{k_{22}} = (E + S_{11}) \frac{L_2^3}{12L_1} + \left(G + S_{22} - \frac{G^2}{G + S_{11}} \right) \frac{L_1 L_2}{12} \quad (15)$$

is the tangent stiffness associated with $\Delta \theta$. The incremental force ΔF_θ can be interpreted as an incremental bending moment ΔM .

We now assume that the strains are small, then the magnitudes of S_{11}, S_{22} are much smaller than E, G . The terms in parentheses in Eq. (15) can be approximated by

$$E + S_{11} \approx E \quad (16a)$$

$$\begin{aligned} G + S_{22} - \frac{G^2}{G + S_{11}} &= G + S_{22} - \left(G \frac{1}{1 + S_{11}/G} \right) \\ &\approx G + S_{22} - G(1 - S_{11}/G) = S_{11} + S_{22} \end{aligned} \quad (16b)$$

so that Eq. (15) becomes

$$k = \left(E + (S_{11} + S_{22}) \left(\frac{L_1}{L_2} \right)^2 \right) \frac{L_2^3}{12L_1} \quad (17)$$

Then using $S_{11} = E \varepsilon_{11}$, $S_{22} = E \varepsilon_{22}$, where $\varepsilon_{11}, \varepsilon_{22}$ are the strains corresponding to the homogeneous deformations, Eq. (17) becomes

$$k = \frac{EL_2^3}{12L_1} \left(1 + (\varepsilon_{11} + \varepsilon_{22}) \left(\frac{L_1}{L_2} \right)^2 \right) \quad (18)$$

Using the bending moment of inertia $I = \frac{L_2^3}{12}$ (for unit thickness), and the incremental curvature $\Delta \chi = \frac{\Delta \theta}{L_1}$ (again assuming small strains since the original value of L_1 is used), we see that the tangent bending modulus is

$$(EI)|_{\text{tangent}} = \frac{\Delta F_\theta}{\Delta \chi} = EI \left(1 + (\varepsilon_{11} + \varepsilon_{22}) \left(\frac{L_1}{L_2} \right)^2 \right) \quad (19)$$

When both the displacements and strains are small, the Green–Lagrange strains are very close to the infinitesimal strains, and the 2nd Piola–Kirchhoff stresses are very close to the Cauchy stresses, so under small displacement / small strain conditions, Eqs. (17) and (19) reduce to

$$k = \left(E + (\tau_{11} + \tau_{22}) \left(\frac{L_1}{L_2} \right)^2 \right) \frac{L_2^3}{12L_1} \quad (20)$$

$$(EI)|_{\text{tangent}} = EI \left(1 + (e_{11} + e_{22}) \left(\frac{L_1}{L_2} \right)^2 \right) \quad (21)$$

where e_{ij} is the infinitesimal strain tensor and τ_{ij} is the Cauchy stress tensor.

The incremental deformation corresponding to the imposed bending is shown in Fig. 2, and we can make the following observations:

4-node element without incompatible modes: The bending modulus of this element can be obtained by setting $\Delta \alpha = 0$, then the tangent bending modulus is given by Eq. (12a):

$$\begin{aligned} (EI)|_{\text{tangent}} &= L_1 k_{11} = \left((E + S_{11}) + (G + S_{22}) \left(\frac{L_1}{L_2} \right)^2 \right) \frac{L_2^3}{12} \\ &\approx \left(1 + \frac{G}{E} \left(\frac{L_1}{L_2} \right)^2 \right) EI \end{aligned} \quad (22)$$

(using small strain assumptions). The tangent bending modulus is seen to be too stiff due to shear locking, and the shear locking effect is worsened as the ratio $\frac{L_1}{L_2}$ increases. This shear locking is the primary motivation for introducing the incompatible modes.

4-node ICM element

- (1) The absence of the shear modulus in Eq. (17) shows that shear locking is not present in the ICM element.
- (2) For zero strains, the tangent bending modulus from Eq. (19) is EI . Of course this result is expected since the purpose of incompatible modes is to represent the case of pure bending.
- (3) There is a critical value of the sum $\varepsilon_{11} + \varepsilon_{22}$, corresponding to a zero tangent bending modulus:

$$(\varepsilon_{11} + \varepsilon_{22})|_{\text{crit}} = -\left(\frac{L_2}{L_1} \right)^2 \quad (23)$$

When $L_1 \gg L_2$, the critical value of $\varepsilon_{11} + \varepsilon_{22}$ is very small, thus the small strain assumptions made throughout this derivation are valid

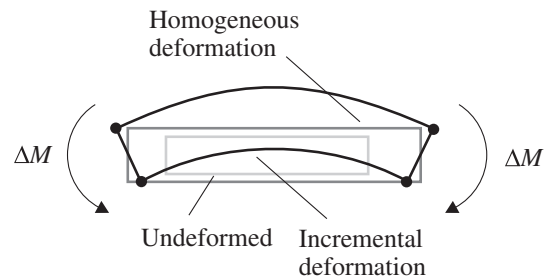


Fig. 2. Total displacements due to incremental bending.

when $L_1 \gg L_2$. We will assume that $L_1 \gg L_2$ throughout our further discussion.

(4) The situation of having only the strain ϵ_{11} nonzero is shown in Fig. 3. The compressive axial force associated with this critical strain is

$$P|_{crit} = (EL_2) \left(\frac{L_2}{L_1} \right)^2 = \frac{12EI}{L_1^2} \quad (24)$$

which compares quite well with the Euler buckling load $P|_{Euler} = \frac{\pi^2 EI}{L_1^2}$ for a beam with both ends pinned. Clearly only an upper bound to the Euler buckling load can be expected, since the bending shape used in the element (Eq. (9)) is only an approximation to the Euler buckling mode shape.

Three-dimensional 8-node ICM element: The corresponding three-dimensional 8-node ICM element contains the same critical strain as the two-dimensional 4-node ICM element (since the two-dimensional incompatible mode shapes are used in the three-dimensional element). For example, considering an undistorted brick element with side lengths L_1, L_2, L_3 , subjected to a compressive strain ϵ_{22} , the critical strain is $\epsilon_{22}|_{crit} = -\left(\frac{L_2}{\max(L_1, L_3)} \right)^2$.

3. Numerical examples

We present in this section the results of various example solutions. These finite element solutions illustrate the results of our simple theory and also show that the instabilities can easily arise in practice. When we refer to strain values, we always mean Green–Lagrange strains, even though these strains are numerically small.

3.1. One element bending tests

The purpose of these tests is to illustrate the results given in Section 2, and to show some of the fundamental characteristics of the responses of different element types.

A single two-dimensional rectangular element is subjected to homogeneous deformation, then incremental bending, as shown in Fig. 4. The element dimensions are shown in Fig. 4a and the element length/width ratio is 10/1. The Poisson ratio is assumed to be zero.

The homogeneous deformation in the longitudinal (horizontal) direction is always applied as a prescribed displacement. The homogeneous deformation in the transverse (vertical) direction is applied in two ways: as a transverse prescribed traction (Fig. 4b), and as a transverse prescribed displacement (Fig. 4c). The incremental rotation is applied as an additional prescribed rotation of $\Delta\theta = 0.001$ radians (Fig. 4d). Combining all of the above, the boundary conditions are

All models:

$$u_1^A = \frac{u}{2} + \frac{L_2}{4} \Delta\theta, \quad u_1^B = -\frac{u}{2} - \frac{L_2}{4} \Delta\theta, \quad u_1^C = -\frac{u}{2} + \frac{L_2}{4} \Delta\theta, \quad u_1^D = \frac{u}{2} - \frac{L_2}{4} \Delta\theta$$

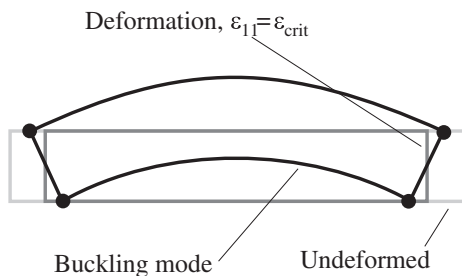
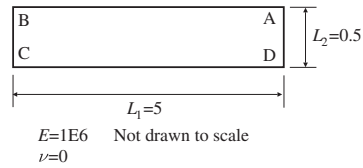
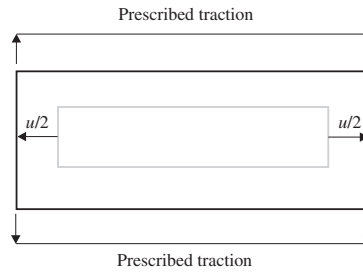


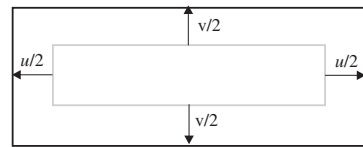
Fig. 3. Buckling mode due to incremental bending.



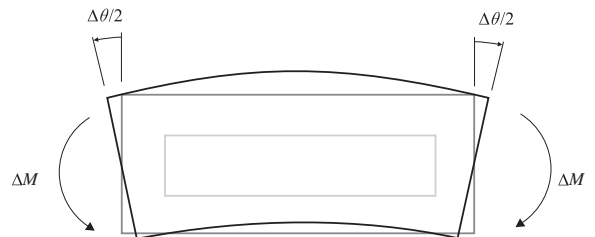
(a) Initial geometry, showing dimensions and nodes



(b) Transverse traction boundary conditions



(c) Transverse displacement boundary conditions



(d) Incremental bending

Fig. 4. One element bending tests.

Transverse prescribed traction:

Traction along line AB = Traction along line CD

Transverse prescribed displacements:

$$u_2 \text{ along line AB} = \frac{v}{2}, \quad u_2 \text{ along line CD} = -\frac{v}{2}$$

In the finite element solution, the general total Lagrangian formulation is used [3], containing as a special case the theory in Section 2. In the first solution step, the homogeneous deformation is applied, and in the second solution step, the incremental rotation is imposed. The conjugate reaction force ΔM obtained from the second solution step is then used to calculate the bending modulus $EI = \Delta M \frac{L_1}{\Delta\theta}$.

Four homogeneous deformation cases are run:

- (1) No deformation: $\epsilon_{11} = \epsilon_{22} = 0$
- (2) $\epsilon_{11} = -0.01, \epsilon_{22} = 0$
- (3) $\epsilon_{11} = 0, \epsilon_{22} = -0.01$
- (4) $\epsilon_{11} = \epsilon_{22} = -0.005$

In cases 2–4, the homogeneous deformations correspond to the critical strain condition given by Eq. (23).

For each homogeneous deformation case, the two transverse boundary conditions of prescribed traction and prescribed displacement are run.

Finally three different element types are used: 4-node elements (without incompatible modes), 4-node ICM elements and quadratic 8-node elements (without incompatible modes).

The results are given in Table 1. In this table, the bending modulus is normalized by the analytical bending modulus $E \frac{I_3}{12} = 1.04167E5$. We observe the following:

- (1) Physically the transverse traction boundary condition should result in a much softer bending modulus than the transverse prescribed displacement boundary condition, since pure bending is permitted with the transverse prescribed traction boundary condition, and pure bending is suppressed by the transverse prescribed displacement boundary condition. We are not trying to accurately compute the bending modulus for the transverse prescribed displacement boundary condition, but we do expect that this bending modulus be much stiffer than the bending modulus corresponding to the transverse traction boundary condition.
- (2) For the 4-node element, the same results are obtained with both transverse boundary conditions, and these results are much stiffer than the analytical beam bending modulus. This result is expected, since the 4-node element does not include a bending deformation shape.
- (3) For the 4-node ICM element, the same results are obtained with both transverse boundary conditions, and these results are in agreement with the theory of Section 2. However the results are physically unrealistic for the transverse prescribed displacement boundary condition. This must be expected, since the displacements corresponding to the incompatible mode do not satisfy the transverse prescribed displacement boundary condition.
- (4) For the 8-node element, the response for the transverse traction boundary condition matches the results from the 4-node ICM element, and the response for the transverse

displacement boundary condition matches the results from the 4-node element. This is all physically realistic.

3.2. Bending of an assemblage of 3 elements, transverse displacement boundary conditions

The assemblage of three elements shown in Fig. 5a is subjected to transverse displacement boundary conditions and incremental rotations, similar to the tests in Section 3.1. The problem dimensions are chosen so that the critical strain is -0.01 , as in Section 3.1. The general total Lagrangian formulation is again employed and the Poisson ratio is assumed to be zero.

The longitudinal strain is always 0. The transverse strain is varied from 0 to -0.01 .

The results are given in Table 2.

4-node element assemblage: For zero transverse strain, the bending modulus is much larger than the analytical beam bending modulus. When the critical strain is imposed in the transverse direction, the bending modulus decreases only slightly.

4-node ICM element assemblage: For zero transverse strain, the bending modulus is about nine times larger than the analytical beam bending modulus. When the critical strain is imposed in the transverse direction, the bending modulus decreases to zero.

The incremental deformations of the 4-node ICM element assemblage are shown, magnified by a factor of 500, in Fig. 5b and c. Fig. 5b shows the actual incremental deformations, including the contribution from the incompatible modes, and Fig. 5c shows the incremental deformations not including the incompatible modes (which is how deformed ICM elements are typically plotted in practice). The corresponding total longitudinal stresses are also shown in Fig. 5c.

Thus we see that the critical strain criterion is applicable to an assemblage of ICM elements, when the adjacent elements can form an interlocking (hour-glass) pattern.

Table 1
Results for the 1-element bending tests.

Element type	Transverse boundary condition	Normalized EI , from calculated solution	Comments
<i>(a) $\epsilon_{11} = \epsilon_{22} = 0$</i>			
4-node	Traction	51.00	51 times the analytical value; result as predicted by equation 22.
4-node	Displacement	51.00	Same result as for transverse traction boundary condition
4-node ICM	Traction	1.00	Same as analytical solution
4-node ICM	Displacement	1.00	Much too soft
8-node	Traction	1.00	Same result as for 4-node ICM element
8-node	Displacement	51.00	Same result as for 4-node element
<i>(b) $\epsilon_{11} = -0.01, \epsilon_{22} = 0$</i>			
4-node	Traction	49.97	Nearly the same result as with $\epsilon_{11} = \epsilon_{22} = 0$
4-node	Displacement	49.97	Same result as for transverse traction boundary condition
4-node ICM	Traction	-0.03	Nearly zero, as predicted by equation 19. This corresponds to Euler buckling.
4-node ICM	Displacement	-0.03	Transverse displacement boundary conditions not matched by incompatible mode.
8-node	Traction	-0.03	Same result as for 4-node ICM element
8-node	Displacement	49.97	Same result as for 4-node element
<i>(c) $\epsilon_{11} = 0, \epsilon_{22} = -0.01$</i>			
4-node	Traction	50.00	Nearly the same result as with $\epsilon_{11} = \epsilon_{22} = 0$
4-node	Displacement	50.00	Same result as for transverse traction boundary condition
4-node ICM	Traction	0.00	Zero, as predicted by equation 19.
4-node ICM	Displacement	0.00	Transverse displacement boundary conditions not matched by incompatible mode.
8-node	Traction	0.00	Same result as for 4-node ICM element
8-node	Displacement	50.00	Same result as for 4-node element
<i>(d) $\epsilon_{11} = \epsilon_{22} = -0.005$</i>			
4-node	Traction	49.98	Nearly the same result as with $\epsilon_{11} = \epsilon_{22} = 0$
4-node	Displacement	49.98	Same result as for transverse traction boundary condition
4-node ICM	Traction	-0.02	Nearly zero, as predicted by equation 19.
4-node ICM	Displacement	-0.02	Transverse displacement boundary conditions not matched by incompatible mode.
8-node	Traction	-0.02	Same result as for 4-node ICM element
8-node	Displacement	49.98	Same result as for 4-node element

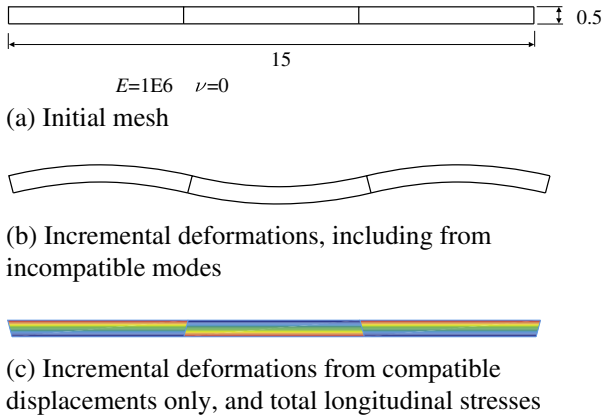


Fig. 5. Bending of an assemblage of elements, transverse displacement boundary conditions.

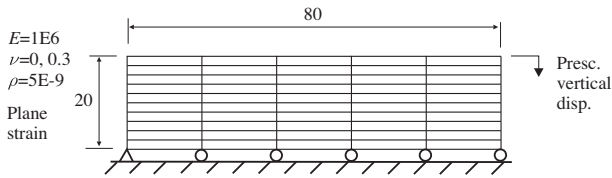


Fig. 6. Frequency analysis of a plane strain compressed block, unconfined in the longitudinal direction.

3.3. Frequency analysis of a two-dimensional compressed block, unconfined in longitudinal direction

The block shown in Fig. 6 is compressed and a frequency analysis is performed in the compressed configuration. A uniform mesh of 4-node ICM elements with the total Lagrangian formulation is employed. A consistent mass matrix is used in the frequency analysis.

As the length to width ratio of the elements is 8/1, the critical strain is 1/64, corresponding to a critical compressive displacement of 0.315.

The lowest two eigenvalues are graphed as a function of the compressive displacement in Fig. 7. At the critical compressive displacement, the lowest eigenvalue becomes negative, and for a slightly larger compressive displacement, the second lowest eigenvalue also becomes negative. The results are in excellent agreement with the theory in Section 2.

The results are affected only slightly by the choice of Poisson's ratio.

Also shown for comparison is the lowest eigenvalue when 4-node elements (without incompatible modes) are used. The eigenvalue decreases only slightly over the range of compressive displacements shown. Again this result is in accordance with theory.

Fig. 8 shows the mode shape and modal longitudinal stresses of the model with ICM elements and zero Poisson's ratio, calculated at the critical compressive displacement. The spurious interlocking (hour-glass) pattern is clearly visible.

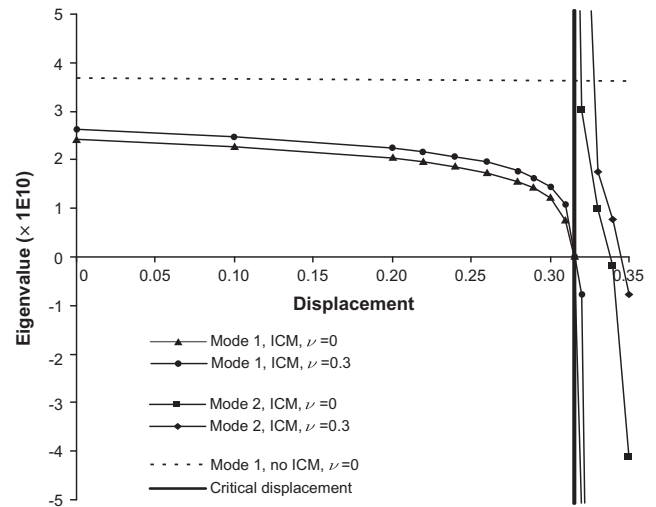


Fig. 7. Eigenvalues vs. compressive displacement for frequency analysis of a 2D compressed block, unconfined in longitudinal direction.

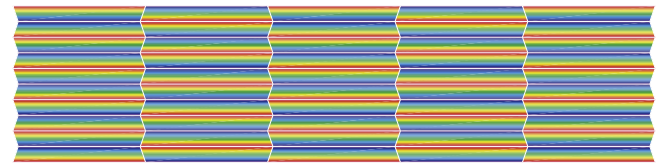


Fig. 8. Spurious mode and modal longitudinal stresses for frequency analysis of a 2D compressed block, unconfined in longitudinal direction.

3.4. Frequency analysis of a compressed block, confined in longitudinal direction

The same problem as in Section 3.3 is solved, except that the block is confined in the longitudinal direction and Poisson's ratio is equal to zero (Fig. 9). Again, a uniform mesh of 4-node ICM elements with the total Lagrangian formulation is employed.

Different mesh refinements, all with the same element length to width ratio of 8/1, are considered. The critical compressive displacement (compressive displacement at which the lowest mode has a zero eigenvalue) is plotted as a function of the number of elements in the mesh (Fig. 10).

The longitudinal boundary condition tends to suppress the interlocking spurious modes, so that the critical compressive displacement is higher than the theoretical value; however, as the mesh is refined, the critical compressive displacement approaches the theoretical value. A typical spurious mode shape and the modal longitudinal stresses are shown in Fig. 11.

3.5. Limit load analysis of a thread in a power screw

Fig. 12 shows a schematic of a power screw, and the thread geometry of the screw. The material of the power screw is idealized as an elastic–plastic material with bilinear isotropic

Table 2
Results for bending of an assemblage of 3 elements, transverse displacement boundary conditions.

Element type	ϵ_{22}	Normalized EI , from calculated solution	Comments
4-node	0	253	
4-node	-0.01	248	
4-node ICM	0	8.84	
4-node ICM	-0.01	0.00	Virtually no stiffness. nonphysical spurious mode

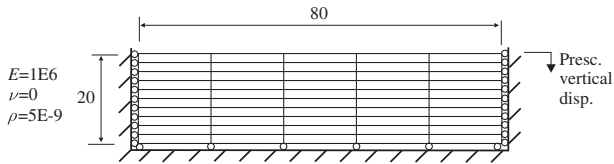


Fig. 9. Frequency analysis of a compressed block, confined in the longitudinal direction.

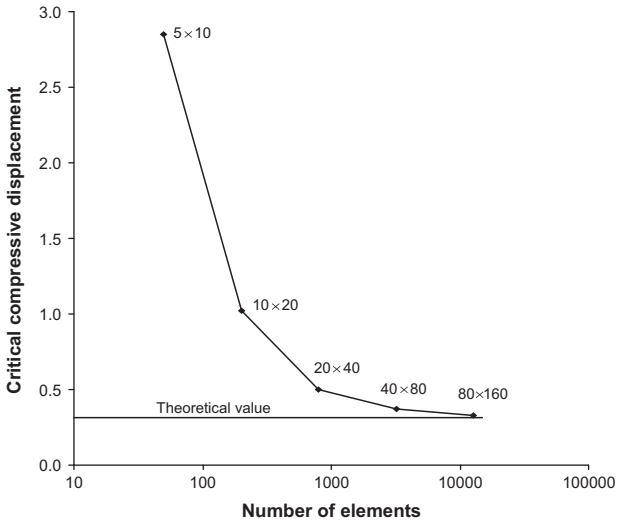


Fig. 10. Results for frequency analysis of the compressed block, confined in the longitudinal direction.

hardening. The nut is idealized as rigid, and frictionless contact is assumed between the screw and the nut.

Fig. 13 shows a three-dimensional model of 180 degrees of the thread. A mesh of 8-node ICM elements is used, along with a few 6-node prism elements, and the total Lagrangian formulation is employed. Notice that the pitch of the thread is included in the mesh.

The aspect ratio of the elements in the thread is quite large, with the elements much longer in the tangential direction than in the other directions. However, it would lead to a very inefficient solution if a mesh with good aspect ratio elements were used for this geometry and in practice meshes with long slender elements are used.

An axial prescribed displacement is applied to the screw, and the thread of the screw contacts the thread groove of the nut.

When the threads come into contact, a plastic zone forms at the fillet between the screw thread and the screw. On further loading, a spurious mode is triggered. This mode can be visualized by plotting (non-smoothed) bands of the effective stresses as shown in Fig. 14.

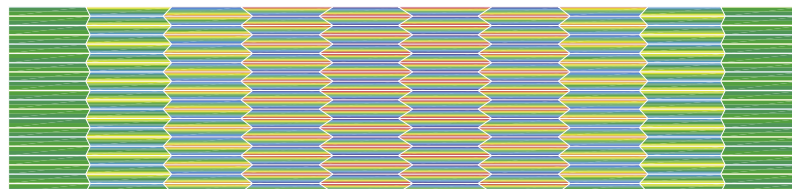
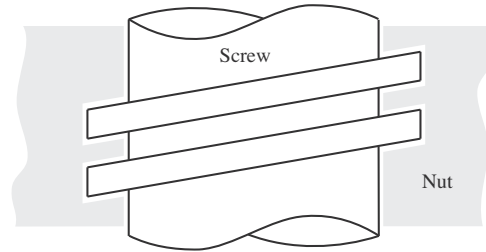
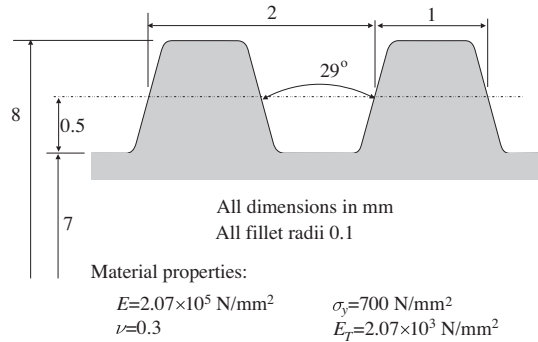


Fig. 11. Spurious mode shape and modal longitudinal stresses for frequency analysis of a compressed block, confined in longitudinal direction.



Not drawn to scale
Lead is equal to twice the pitch.

(a) Schematic drawing of power screw



(b) Thread geometry and material properties

Fig. 12. Power screw geometry.

The effect of the spurious mode is also evident in the force-displacement curve (Fig. 15), in which we see that the force drops suddenly when the spurious mode is triggered. For comparison, in Fig. 15, we also give the results obtained when the ordinary 8-node element is used (that is, when incompatible modes are not included), and when a mixed displacement/pressure formulation is used with the 8/1 element. Here, the 8 corner nodes are used for the displacement interpolation and 1 pressure degree of freedom is employed [3]. Notice that the ordinary 8-node element mesh is too stiff, which we expect since plasticity is occurring, plastic strains are incompressible and therefore volumetric locking occurs in the ordinary 8-node element. The 8/1 element is formulated to alleviate volumetric locking, and the mesh gives results almost identical to the 8-node ICM element mesh until the spurious mode in the ICM element assemblage is triggered.

Clearly the contact surfaces and surrounding elements are acting as displacement boundary conditions on the ICM elements, and the incompatible displacements in the ICM elements are not compatible with the displacement boundary conditions.

This problem demonstrates that a spurious mode can occur in practical finite element analysis involving only small displacements when using the ICM elements.

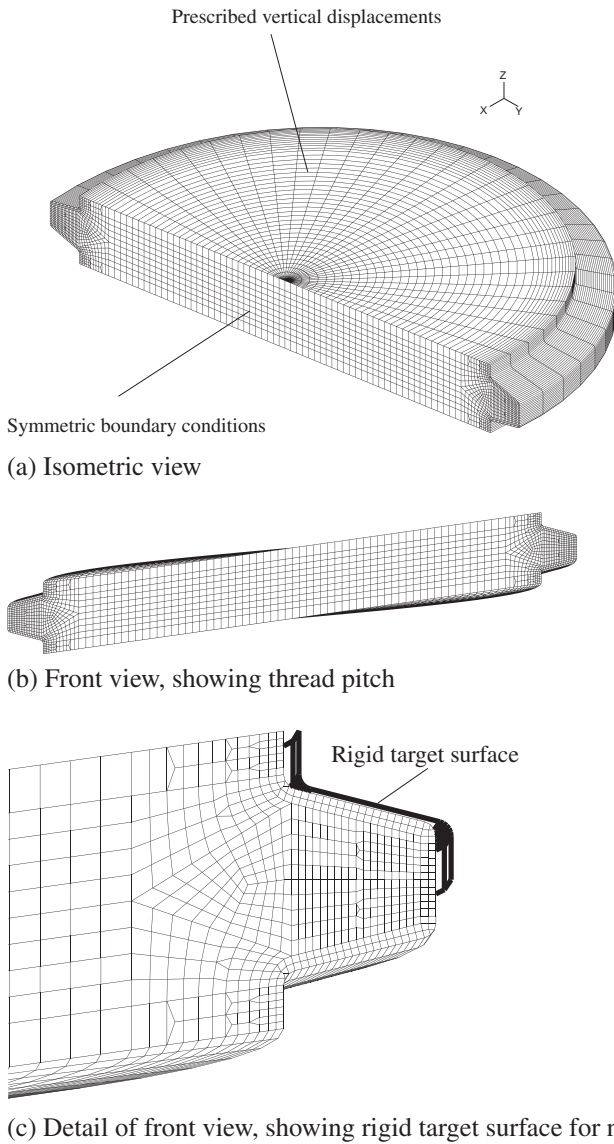


Fig. 13. 3D finite element mesh of power screw.

4. Concluding remarks

While the difficulties of using elements with incompatible modes in large strain analyses are well known, we considered in this paper geometrically nonlinear elements subjected to only small strains and small displacements. This is clearly a very large field of analysis.

In Section 2, we derived the tangent bending modulus of the geometrically nonlinear 4-node ICM element with the following simplifying assumptions: undistorted rectangular element, linear elastic material, zero Poisson’s ratio, and small strains. These simplifications were made to obtain basic insight into the element behavior. The same derivation can also be performed with a non-zero Poisson’s ratio, but the effect of Poisson’s ratio is small (as long as no incompressible confined material condition is approached), the resulting formulas are more complex and little further insight is gained.

When the tangent bending modulus is zero in the presence of only transverse traction boundary conditions, Euler buckling is seen, the associated mode shape is a physical response and hence is not spurious. But when the tangent bending modulus is zero in

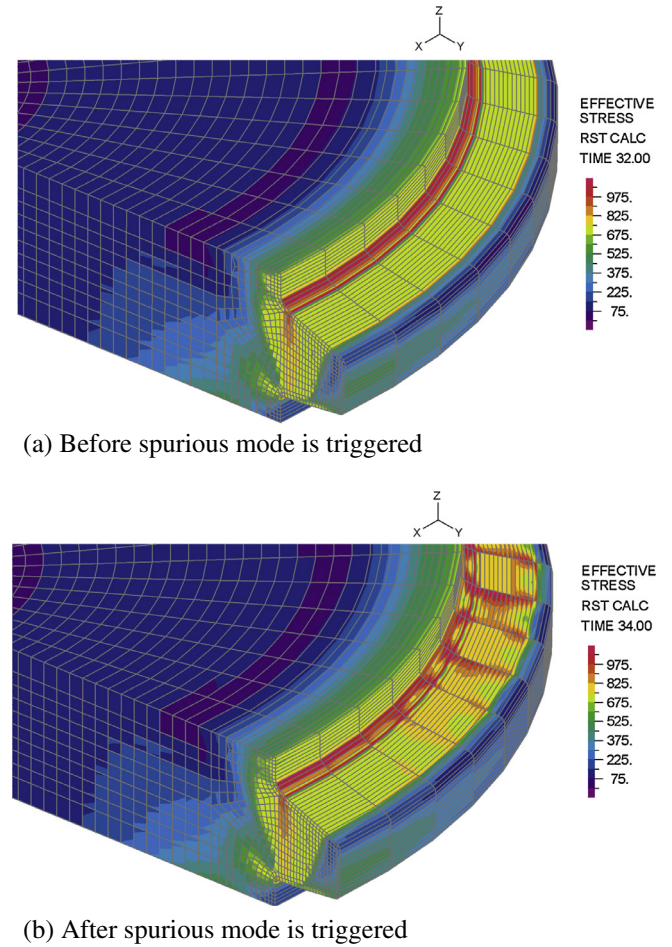


Fig. 14. Effective stresses in power screw mesh.

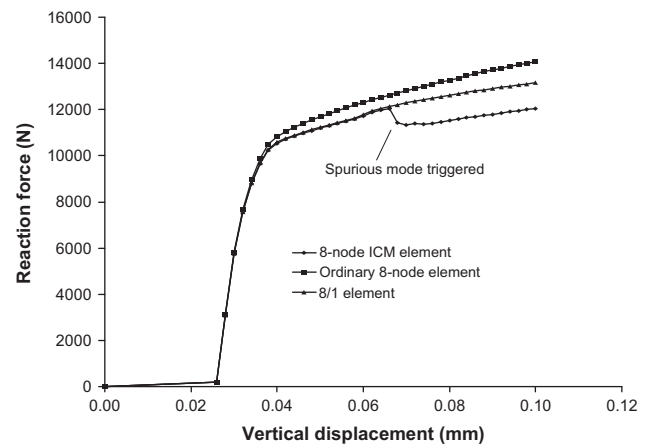


Fig. 15. Force–deflection curves for power screw model.

the presence of transverse displacement boundary conditions, a nonphysical response is seen: the zero tangent bending modulus then corresponds to a spurious mode.

It is clear from the derivation that the spurious modes are inseparable from the desirable characteristics of the ICM elements, namely the absence of shear locking, and that the spurious modes

are a direct consequence of the incompatibility of the incompatible modes with prescribed displacement boundary conditions.

In Section 3, we illustrated the nonphysical response obtained with the ICM elements. All these results are in correspondence with the developed simple theory, and show that the element deficiency might be widely seen in actual finite element solutions (if element aspect ratios are large). The fundamental reason is that ICM elements are in practice embedded within finite element meshes where for a typical element, the neighboring elements and contact conditions provide in essence displacement boundary conditions.

We did not investigate in this paper whether there are additional deficiencies of the ICM elements due to element geometric distortions, but focused on the simplest case for a theoretical analysis.

Based on the experiences presented in this paper, we recommend that the ICM elements be used with caution in geometric nonlinear analyses, even involving only small strains, and that when the ICM elements are used, these elements do not have a large geometric aspect ratio.

References

- [1] Wilson, EL, Taylor RL, Doherty WP, Ghaboussi J. Incompatible displacement models. In: Fenves SJ et al., editors. Numerical and computer methods in structural mechanics. Academic Press; 1973. p. 43–57.
- [2] Wilson EL, Ibrahimbegovic A. Use of incompatible displacement models for the calculation of element stiffness and stresses. *Finite Elem Anal Des* 1990;7:229–41.
- [3] Bathe KJ. *Finite element procedures*. Prentice Hall; 1996.
- [4] Simo JC, Rifai S. A class of mixed assumed strain methods and the method of incompatible modes. *Int J Numer Meth Eng* 1990;29:1595–638.
- [5] Simo JC, Armero F. Geometrically non-linear enhanced strain mixed methods and the method of incompatible modes. *Int J Numer Meth Eng* 1992;33:1413–49.
- [6] Büchter N, Ramm E, Roehl D. Three-dimensional extension of nonlinear shell formulation based on the enhanced assumed strain concept. *Int J Numer Meth Eng* 1994;37:2551–68.
- [7] Pantuso D, Bathe KJ. A four-node quadrilateral mixed-interpolated element for solids and fluids. *Math Models Methods Appl Sci* 1995;5(8):1113–28.
- [8] deSouza Neto EA, Peric D, Huang GC, Owen DRJ. Remarks on the stability of enhanced strain elements in finite elasticity and elastoplasticity. *Commun Numer Methods Eng*. 1995;11:951–61.
- [9] Wriggers P, Reese S. A note on enhanced strain methods for large deformations. *Comput Methods Appl Mech Eng* 1996;135:201–9.
- [10] Pantuso D, Bathe KJ. On the stability of mixed finite elements in large strain analysis of incompressible solids. *Finite Elem Anal Des* 1997;28:83–104.
- [11] Wall W, Bischoff M, Ramm E. A deformation dependent stabilization technique, exemplified by EAS elements at large strains. *Comput Methods Appl Mech Eng* 2000;188:859–71.
- [12] Bathe KJ. *Advances in the Multiphysics Analysis of Structures*. In: Topping BHV, editor. Chapter 1 in *Computational methods for engineering science*. Stirlingshire, Scotland: Saxe-Coburg Publications; 2012.